Editors' Suggestion

Damage separation model: A replaceable particle method based on strain energy field

Yupeng Jiang [1,*] Peter Mora,[2] Hans J. Herrmann,[3] and Fernando Alonso-Marroquín[1]
[1]*School of Civil Engineering, The University of Sydney, Sydney 2006, New South Wales, Australia*
[2]*College of Petroleum Engineering and Geosciences, King Fahd University of Petroleum and Minerals, Dhahran 31261, Saudi Arabia*
[3]*PMMH, ESPCI, 17 Quai St. Bernard 75005, Paris, France*

(Received 10 March 2021; accepted 20 September 2021; published 25 October 2021)

We present a realistic model for simulating particle fragmentation in granular assemblies, the damage separation model (DSM), that addresses the limitations of previous methods by replacing the particle with smaller ones after fragmentation. The method is based on the calculation of the strain energy field inside the particle, and it solves the two major issues of the existing replaceable particle methods: the oversimplification of particle stress, and the unrealistic geometrical constraints needed in postbreakage replacements. Our model is formulated with three modules: (i) a boundary element calculation of stress and strain fields inside the spheropolygons that represent individual particles; (ii) a strain-energy-based theoretical framework to determine the onset of fragmentation; and (iii) an advanced geometrical algorithm, the subset separation method (SSM), to handle the postbreakage replacements in the discrete element simulations. Especially, the SSM effectively calculates the fragments required by the replacement with no geometrical limitation on the number, location, and orientation of the fracture planes. A uniaxial compression test based on laboratory setups is used to validate the method. A comparison is further conducted to study the performance of four different replaceable irregular particle methods. Results indicate that our method overcomes most of the existing issues, including stability, accuracy, and artificial constraints on the number and shape of fragments. The DSM has great potential for capturing the morphological changes of particle breakage and comminution with an unprecedented numerical resolution.

DOI: 10.1103/PhysRevE.104.045311

I. INTRODUCTION

Particle breakdown occurs in granular media when there is sufficient external loading. For example, in fault zones there is a continual breakdown of the fractured zone or fault gouge layer, leading to a power-law distribution of particle sizes. At the microscale, the shape [1,2] and the size of each broken particle [3–5] change as particles break down. At the mesoscale, the contact force chains are disturbed and quickly rearranged after the breakage events, which changes the distribution of the local mechanical energy. At the macroscale, the particle breakage causes a variation in density [6], compressibility [7], and elastic modulus. The effects of particle breakage have been comprehensively studied through many experiments [1–3,7], which have built a solid foundation for understanding particle breakage. These studies focused on the changes of the state variables at the macroscale, such as the particle size distribution (PSD) and normal compression line (NCL) [6], under different loading conditions.

The study of particle breakage at the grain scale is often numerically simulated with the discrete element method (DEM) [8–11]. This method provides comprehensive information about the evolution of the force chains and the locations of strongly loaded particles, which are difficult to observe in laboratory experiments. The DEM-based breakage methods have been systematically developed due to these advantages. Based on the features of their algorithms, existing methods can be summarized into two paradigms: agglomerates and replaceable particles [10]. The replaceable particle method considers each grain as a single entity [12–16]. The breakage of the original particle is achieved by replacing the original particle with new fragments if a specified breakage criterion is fulfilled. For the agglomerates method [9,17–22], each particle consists of many small particles that are bonded together through predefined forces, thereby giving an approximation to the continuum stress state of the agglomerate particle. Under external loading, a bond within the agglomerate may break once certain thresholds are reached. This strategy eventually causes the total breakdown of the agglomerates into its constituents, at which time no further breakage is allowed.

The agglomerates method is regarded as a less favorable method since it is computationally much less efficient than the replaceable particle method while not clearly showing better accuracy [10]. The replacement particle method has the highest efficiency, and results of PSD and NCL are also in good agreement with experimental findings [10]. However, the breakage criteria are based on the calculation of the averaged stress tensor on each particle. This approach does not correctly model the breakage of an arbitrarily shaped grain [23]. Specifically, it is commonly used to break down a circular particle (in two dimensions) into other circular particles. This leads to two major problems after the replacement because the particles are limited to a circular shape: The conservation of mass cannot be guaranteed, and local contact forces experience a discontinuous change that causes computational instability and an energy jump in the granular material. These problems can be solved by using irregular particles, such as polygons, but this leads to a tradeoff between computational efficiency and accuracy of the PSD. The

*Corresponding author: amosjiang@outlook.com

disadvantages of using replaceable particles arise from the dependency on the oversimplification of the particle stress state. The averaged stress tensor cannot accurately capture the inner particle stress state before the breakage, and hence it cannot accurately predict the breakage of the particle. As such, it is difficult to properly determine the shape of the new fragments from the averaged stress tensor. Hence, artificial constraints on the number and the orientation of the fracture planes are required by the replacement particle strategies.

In this work, we develop a replaceable particle method, namely the damage separation method (DSM), that could largely solve the aforementioned problems. The method is based on our previous boundary spheropolygon element method (BSEM) formulation [23,24]. This is a combination of the spheropolygon discrete element method (SDEM) [25,26]—a discrete element method that handles the dynamics of spheropolygons—and the boundary element method (BEM)—a continuum method to calculate the stress field inside particles. First, we extend the BSEM method to resolve the fragmentation using the strain energy formulation discussed in [27]. In this formulation, the fragmentation patterns are obtained based on the numerical determination of the ridges of strain energy field inside the particle. The generation of the child fragments from the parent particle after fragmentation requires a new algorithm that we define as the subset separation method (SSM). After integrating the different algorithms, the DSM achieves full coupling between the discrete particles and the continuum field inside them, which effectively replaces the broken particles at each time step based on their strain energy field.

A validation test for the DSM is performed, and the results are rigorously compared against the experiments of Cantor *et al.* [15]. Then a series of simulations of an oedometric test are conducted to compare the DSM with three existing replaceable particle methods. The comparison and analysis mainly focus on the following aspects: (i) morphological changes of particles [28], (ii) spatial distribution of breakage events and their relationship with the contact force chain, and (iii) particle size distribution curves. Simulation results indicate that the DSM overcomes the crucial problems of stability, accuracy, and artificial constraints on postbreakage replacements in the existing methods.

The paper is organized as follows: the methodology of the three modules is presented in Sec. II. The validation with the pentagonal packing is conducted in Sec. III. A comparison study of different replaceable particle methods using Voronoi particles is provided in Sec. IV. The conclusions are made in Sec. V.

II. METHODOLOGY

In this section, we formulate the framework for the DSM, which covers the three key modules, namely the BSEM method for calculation of strain energy field, the theoretical framework for particle fragmentation based on strain energy, and the SSM postbreakage replacement algorithm. The first two modules are direct implementations of our methods presented in [23,24] and [27]. Therefore, we mainly focus on showing their concepts, functionalities, and incorporation in the DSM. The formulation of the postbreakage algorithm (SSM)—the key innovation and most critical component of the DSM—is presented in detail in this paper.

A. Calculation of the particle stress field using the boundary spheropolygon element method

We first introduce the module to calculate the strain energy field on the particle, i.e., the BSEM. It couples the spheropolygon element method—a discrete method for irregular particle dynamics—and the boundary element method—a continuum method for inner particle stress calculation—to govern the breakage process in a far more accurate way than when using the averaged stress tensor. The framework of the BSEM is summarized in Figs. 1(a)–1(c) by taking a loaded irregular particle under equilibrium as an example.

To calculate its stress field, we first generally consider the particle—under its local coordinate system (x, y)—as a linearly elastic, homogeneous domain Ω confined by its boundary Γ, i.e., Fig. 1(b). The domain is subjected to the displacement boundary $\boldsymbol{u}(\boldsymbol{x}) = \bar{\boldsymbol{u}}$ for $\boldsymbol{x} \in \Gamma_u$ and traction boundary $\boldsymbol{t}(\boldsymbol{x}) = \bar{\boldsymbol{t}}$ for $\boldsymbol{x} \in \Gamma_t$ with $\Gamma_u \cup \Gamma_t = \Gamma$ and $\Gamma_u \cap \Gamma_t = \emptyset$. Notably, the boundary condition for the particle is purely traction-based.

We then apply the standard boundary integral equation [23], and we obtain its discretized form using N constant boundary elements generated along the outer edges of the particle as shown in Fig. 1(c). By assembling the discretized elements, one can obtain the matrix equation $\boldsymbol{AU} = \boldsymbol{BT}$, where $\boldsymbol{U} = [\boldsymbol{u}_1, \boldsymbol{u}_2, \ldots, \boldsymbol{u}_N]$ and $\boldsymbol{T} = [\boldsymbol{t}_1, \boldsymbol{t}_2, \ldots, \boldsymbol{t}_N]$ are the assembled elemental displacement and traction vector, respectively, and the coefficient matrices $\boldsymbol{A}$ and $\boldsymbol{B}$ are constructed using the fundamental solutions as explained in [23].

Next, we import the contact forces into the traction vector $\boldsymbol{T}$. Based on the axial projection of contact location in (x, y), a contact force $\boldsymbol{f}$ is assigned to the corresponding boundary elemental traction vector after being divided by the length of the element. As presented in Fig. 1(c), the contact forces $\boldsymbol{f}_\alpha$ and $\boldsymbol{f}_\beta$ are assigned to their corresponding boundary elements as $\boldsymbol{t}_\alpha$ and $\boldsymbol{t}_\beta$. The contact-free elements have a zero value for their traction vectors. Since $\boldsymbol{T}$ is now determined through the contact forces, the matrix equation can be easily solved by inverting the coefficient matrix $\boldsymbol{A}$ to obtain the unknown vector $\boldsymbol{U}$. The field of Cauchy stress $\sigma(\boldsymbol{x})$ can then be calculated as

$$\sigma_{ij}(\boldsymbol{x}) = \int_\Gamma D_{kij}(\boldsymbol{x}) t_k d\Gamma - \int_\Gamma S_{kij}(\boldsymbol{x}) u_k d\Gamma \ (i, j, k = 1, 2), \quad (1)$$

where D_{ijk} and S_{ijk} are the Kelvin fundamental solutions [23]. Based on Eq. (1), the elastic strain energy density can be conveniently calculated, which will be used for the determination of fragmentation in the second module.

B. Fragmentation criteria based on particle strain energy field

We address the second module after the completion of the BSEM, namely the fragmentation based on the strain energy field [27], which is illustrated in Figs. 1(d)–1(f). The fragmentation of a particle is the coalescence of its inner damaged domains caused by the increase of local strain energy. This advanced theory allows one to determine both the occurrence of breakage and fracture planes using an equivalent stress ψ associated with elastic strain energy $W_e = \psi^2/2E$, which is

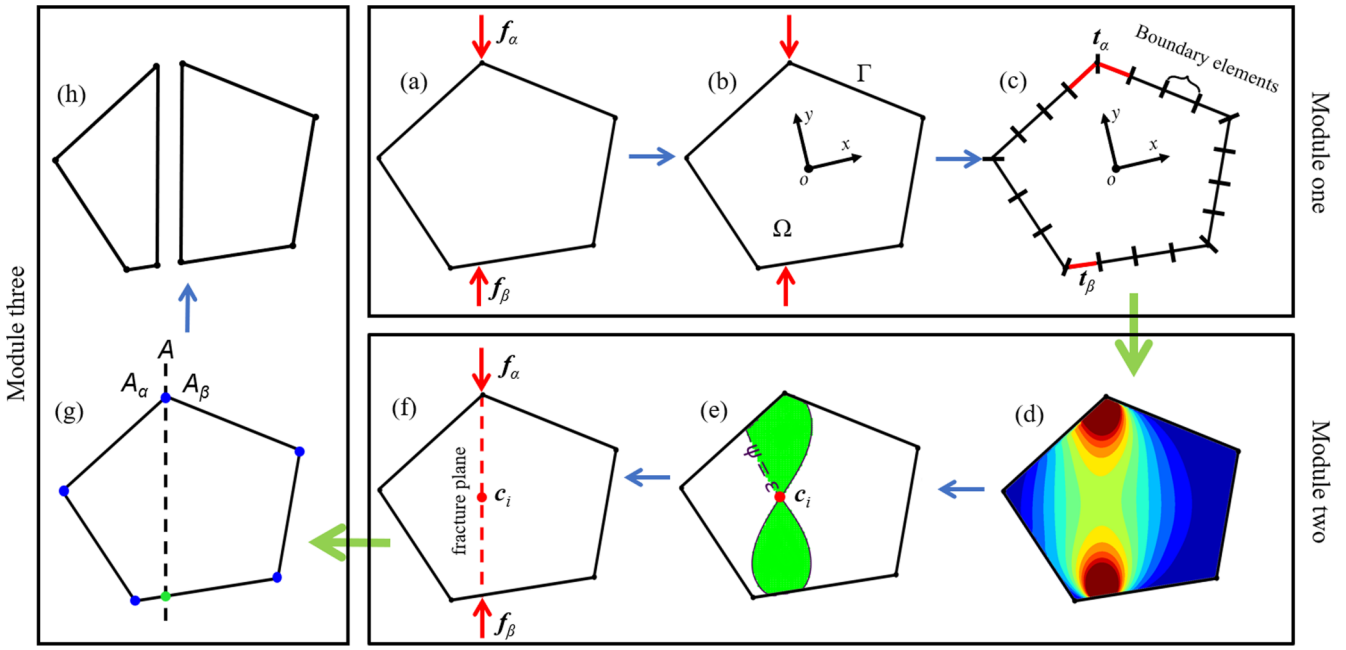

FIG. 1. The three modules of the computational framework of inner particle stress and fragmentation calculation. (a) A loaded particle is in equilibrium with a pair of contact forces $\boldsymbol{f}_\alpha$ and $\boldsymbol{f}_\beta$; (b) the particle is represented as a continuum domain with a local coordinate system; (c) the particle boundary is discretized, and the boundary tractions $\boldsymbol{t}_\alpha$ and $\boldsymbol{t}_\beta$ are assigned to the corresponding elements (red lines); (d) the elastic strain energy field is calculated; (e) the damage domains (in lime) and a connection point $\boldsymbol{c}_i$ (red dot) are calculated; (f) the fracture plane (red dashed line) is determined; (g) the subset separation method is applied to the polygon; (h) the polygon is separated into two polygonal fragments.

written as

$$\psi(\boldsymbol{\sigma}, \nu) = \sigma_v \left[\frac{2}{3}(1+\nu) + 3(1-2\nu)\left(\frac{\sigma_m}{\sigma_v}\right)^2 \right]^{1/2}, \qquad (2)$$

where σ_v and σ_m denote von-Mises and hydrostatic stress, respectively, E is Young's modulus, and ν is Poisson's ratio. Demonstration of the elastic strain energy field inside a particle is shown in Fig. 1(d).

We first determine the breakage criterion satisfying

$$\begin{aligned} \psi(\boldsymbol{\sigma}, \nu)|_{\boldsymbol{c}_i} &= \epsilon, \\ \|\nabla\psi|_{\boldsymbol{c}_i}\| &= 0, \end{aligned} \qquad (3)$$

where ∇ is the gradient operator, ϵ is the lower bound of ψ that delimits the damaged domains, which is lime-colored in Fig. 1(e), and P_i is the location where damaged (colored) domains first coalesce, which is called the *connection point* and is denoted by the red dot in Fig. 1(e). In this work, we fully adopt this criterion to determine the breakage of irregular particles.

Next, we retrieve the fracture planes using the connection and contact points. We define the fracture planes as straight lines between a pair of contact points. This simplification greatly reduces the complexity of geometrical handling while providing a good approximation for the ridges of the strain energy topography [29,30], which was used by the previous theory [27].

For replacing a particle that is deemed broken, a series of connection lines are first made between any pair of contact points. These lines are regarded as potential fracture planes. To handle the potential nonexact collinearity between the connection lines and points, we define that an actual fracture plane is a connection line that has the minimum point-to-line-distance with a connection point. The number of connection points equals that of fracture planes. Taking Fig. 1(f) as the example, the connection line is generated to link the contact points of $\boldsymbol{f}_\alpha$ and $\boldsymbol{f}_\beta$. It is then further determined as a fracture plane due to the location of $\boldsymbol{c}_i$. In this way, the fracture planes are generated for the calculation of replacements in the next module.

It needs to be noted that the numerical examples in the original study [27] were conducted using circular particles. However, the theory imposes no constraint on particle geometry. This is because the theory was developed only based on Griffith's elastic fracture mechanics and elastic strain energy with no assumption of the domain shape. Hence, the theory is also applicable to irregularly shaped particles.

C. Subset separation method

We introduce the last module of the DSM in this section, namely the subset separation method, which subdivides a particle based on its fracture planes, as shown in Figs. 1(g) and 1(h). To better understand the advantages of the SSM, we first revisit the limitations and numerical challenges of existing replacement methods.

Replacing the original particle with its broken parts is the crucial step for the breakage algorithm. Its application to noncircular particles could effectively avoid problems such as loss of mass and numerical discontinuity of contact forces, which is inevitably produced by the replacement method of circular particles. However, the separation of an arbitrary polygon is

geometrically challenging. It is highly difficult to calculate all the possible scenarios for the breakdown of particles into new particles because of uncertainty in the orientation and the number of fragmenting lines. The existing replacement methods for irregular particles are limited to the case of separating the polygon with a fixed number of straight fragmenting lines that all cross through its original geometrical center [14–16]. In this case, the orientation of the fragmenting lines is the only unknown variable that is obtained from the averaged stress tensor of the particle. These separation modes are not ideal for the replacement of fragments based on the inner particle stress state because they introduce artificial constraints on the number and geometry of new fragments and therefore compromise the accuracy of the breakage simulation.

In this paper, we develop a polygon separation algorithm, the SSM, for the replacement of original particles. The algorithm has no limitation on the shape of the particle, the number, and the orientation of the fragmenting lines, or the constraint of the original geometrical center. The separation of the particle is only defined by straight fragmenting lines with no other artificial constraints applied. Convex polygons are used here as a demonstration of the SSM, but it can be equally applied to the concave polygons after dividing the concave polygon into convex subdomains.

The principle of the SSM algorithm is to find the vertices of each new polygon fragment using the intersection of subsets defined by the fracture planes. These vertices are taken from three types of points generated by the fracture planes (Fig. 2): the vertices of the original polygon (blue dots), the intersection points between a fracture plane and the polygon's boundary (green dots), and the intersection points between pairs of fracture planes (red dots). We define here the collection of all these points as the *Set*. If two points spatially coincide with each other, they will not be repeated in the set due to its mathematical definition.

The second step of the SSM algorithm is to construct the subsets. As we can see from Fig. 2(a), a fracture plane A separates the blue dots into two groups, one above and one below, and thus generates two *Subsets*, namely A_α and A_β. The points (blue dots) above or on A are assigned to subset A_α, and those below or on A are assigned to A_β. The points located at A (green dots) are assigned to both A_α and A_β. This location-based rule is also applied for the red dots in Figs. 2(b) and 2(c). The subsets generated by B (B_α, B_β) and C (C_α, C_β) in Figs. 2(b) and 2(c) are generated in the same way. Based on this rule, we obtain a collection of $2n$ subsets, where n is the number of fracture planes.

The third step is to calculate the intersection between any two subsets to obtain the new subsets S_i that contain the vertices of new polygons. The equations for $n = 2$ and 3 in Figs. 2(b) and 2(c) can be written as follows:

$$n = 2, S_{1-4} = \begin{cases} S_1 = A_\alpha \cap B_\alpha, S_2 = A_\alpha \cap B_\beta, \\ S_3 = A_\beta \cap B_\alpha, S_4 = A_\beta \cap B_\beta, \end{cases} \tag{4}$$

$$n = 3, S_{1-8} = \begin{cases} S_1 = A_\alpha \cap B_\alpha \cap C_\alpha, S_2 = A_\alpha \cap B_\alpha \cap C_\beta, \\ S_3 = A_\alpha \cap B_\beta \cap C_\alpha, S_4 = A_\alpha \cap B_\beta \cap C_\beta, \\ S_5 = A_\beta \cap B_\alpha \cap C_\alpha, S_6 = A_\beta \cap B_\alpha \cap C_\beta, \\ S_7 = A_\beta \cap B_\beta \cap C_\alpha, S_8 = A_\beta \cap B_\beta \cap C_\beta, \end{cases} \tag{5}$$

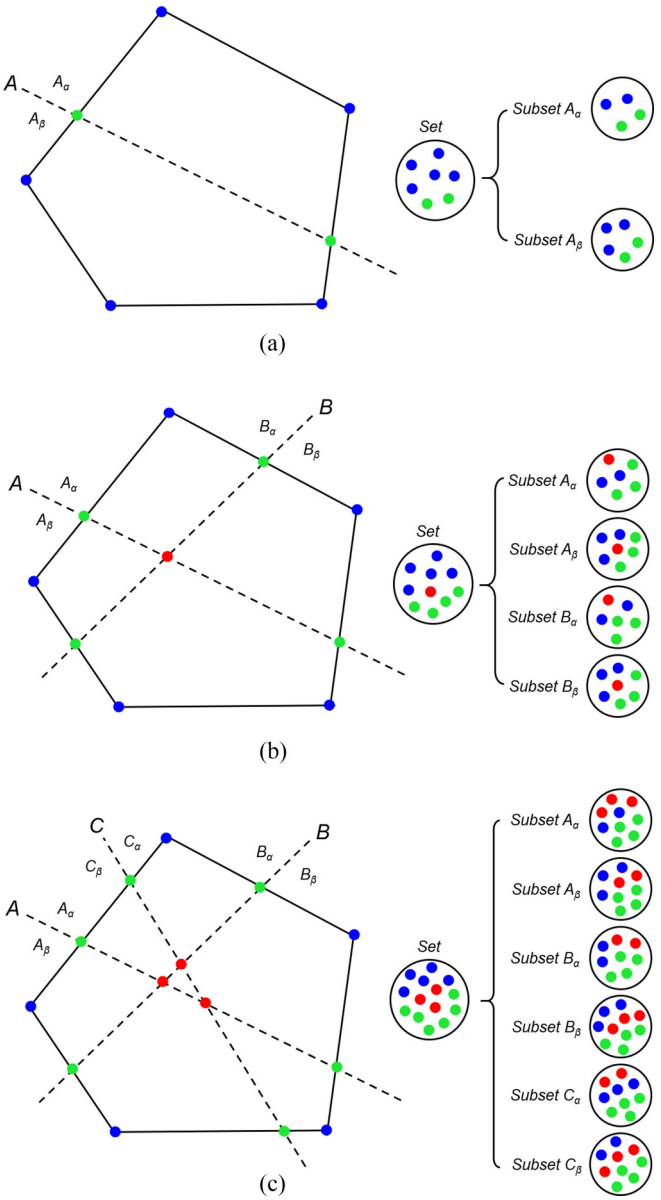

FIG. 2. A polygon with a different number of fragmenting lines and the resultant set/subsets generated by the fracturing lines. The blue nodes denote the vertices of the original polygon; the green dots are at the end points of the fragmenting lines; the red dots represent the intersection points of the fragmenting lines. (a) $n = 1$, (b) $n = 2$, and (c) $n = 3$.

where a total number of 2^n S_i are obtained. A polygon P_i is defined if the number of points in its corresponding intersection subset S_i is larger than 2. As illustrated in Fig. 3, the intersection subset S_1 in Eq. (5) is obtained by intersecting A_α, B_α, and C_α. Since S_1 contains four points, the polygon P_1 can be defined using these points as its vertices. To generate P_1, the points in S_1 need to be put into the right sequence since a set (or subset) mathematically does not have a defined sequence for its points. We first average the original coordinates of the points in S_1 with the total number of points ($|S_1|$). These points are then arranged in a counterclockwise order by sorting the angle created by each point with the centroid. In this way, the

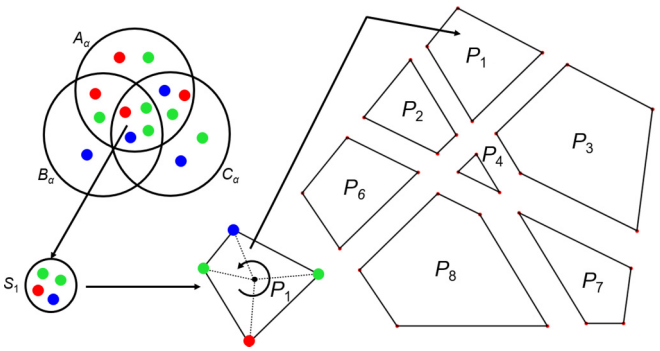

FIG. 3. The new polygons created by the fragmenting lines are calculated from SSM. The workflow for the generation of the polygon subsets is presented. The polygon P_5 does not exist since it corresponds to the intersection subset S_5, which is empty.

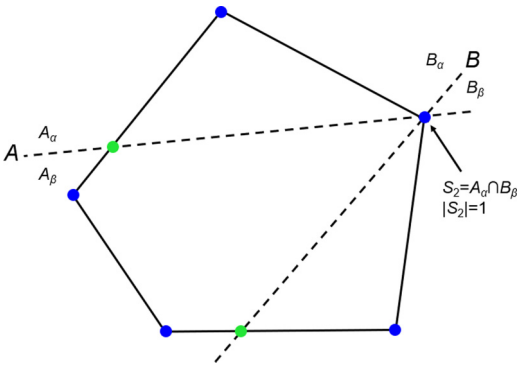

FIG. 4. The situation in which the intersection subset only contains one point and does not construct a new polygon.

polygon P_1 can be generated numerically for the replacement. This rule is applied to all subsets S_i.

It is noted that a polygon P_i will not exist if its corresponding intersection subset S_i is empty (i.e., $|S_i| = 0$). For example, the subset S_5 in Eq. (5) contains no points since the intersection between A_β, B_α, and C_β is empty and thus does not form a new polygon. Another scenario for an invalid polygon is when an intersection subset S_i only contains one point (i.e., $|S_i| = 1$). As illustrated in Fig. 4, both A and B cut across the same vertex of the original polygon. The intersection subset S_2, according to Eq. (4), does not construct a new polygon, yet it still contains one point, which is marked out with the black arrow. Either way, these invalid scenarios of intersection subsets can be easily removed with the condition of $|S_i| > 2$, which preserves the robustness of the SSM.

The same algorithm to find the subsets and polygons can be equally extended to the situation with multiple fragmenting lines $n = N$ as

$$n = N, S_{1-2^N} = \begin{cases} S_1 = \underbrace{A_\alpha \cap B_\alpha \cap \cdots \cap N_\alpha}_{N}, S_2 = A_\alpha \cap B_\alpha \cap \cdots \cap N_\beta, \\ \cdots \\ S_{2^{N-1}} = A_\beta \cap B_\beta \cap \cdots N_\alpha, S_{2^N} = A_\beta \cap B_\beta \cap \cdots N_\beta. \end{cases} . \tag{6}$$

Algorithm 1. provides the steps required to calculate the new polygons from the Set with arbitrary numbers of fracture planes. As shown in Fig. 5, the SSM properly handles the situations of $n = 4$ and 5. It needs to be pointed out that the SSM cannot be directly applied to a nonconvex polygon since the number of subsets produced by one fragmenting line may be larger than 2. However, this problem can be solved by first dividing the nonconvex polygon into a series of convex polygons [31]. Then, the SSM is applied to each convex polygon to obtain the intersection of subsets. The new polygons created by the fragmenting lines can be obtained by merging these subsets if their mutual boundaries exist.

D. Considerations on numerical stability

In addition to the three modules, we further provide a numerical treatment for using spheropolygon erosion to improve the numerical stability while properly approximating the physical process of particle rearrangement in the post-breakage stage.

The layout of particles before and after the breakage is shown in Fig. 6. One can see that the new spheropolygons, i.e., fragmented particle A and new particle C, are eroded to a state in which the original contact force—between particle A and B—vanishes due to the zero overlapping distance. In reality, the local contacts are dissipated after breakage, and the fragments are rearranged. This replacement approach

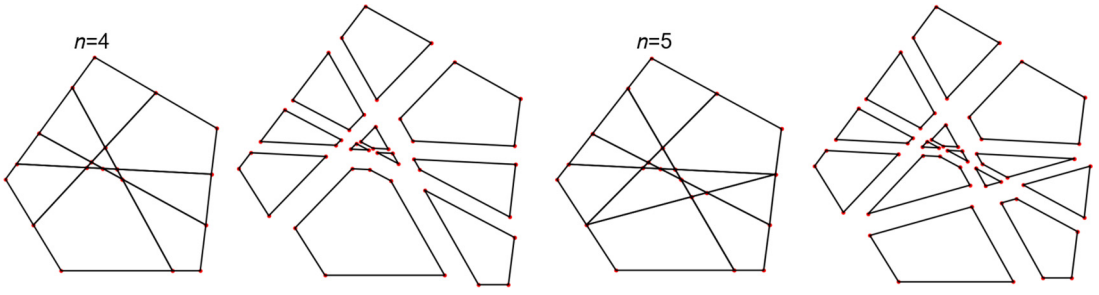

FIG. 5. Examples of $n = 4$ and 5 calculated by the subset separation method.

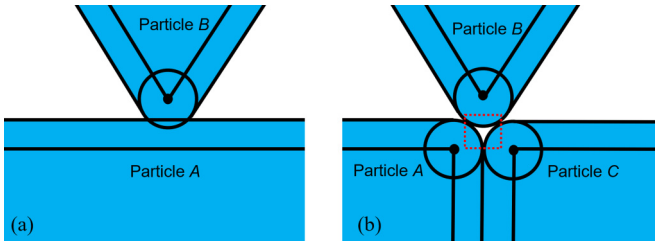

FIG. 6. The contact layout of the original particle and the new fragment. (a) The vertex is in contact with the boundary before the breakage; (b) the breakage occurs and the new particles are inserted and eroded as spheropolygons; loss of mass is marked out with the dashed red square.

could approximate this dissipation and allow the particle to be pushed to its new equilibrium state while the local contact returns to a stable state.

This treatment is also numerically robust as initial overlaps may apply excessive contact forces on the new replacements, which harms simulation stability. The loss of mass, as marked out with the dashed red square in Fig. 6(b), caused by this geometrical change is inevitable yet trivial compared with the mass of the whole particle.

E. DSM numerical procedures

The complete program of the DSM was developed using the C++ language for further validation and application. The numerical procedures within one-time step Δt correspond to an extension of our previous BSEM algorithm and can be summarized as follows:

(i) Contact detection and force calculation of the spheropolygon particles.

(ii) Update the velocity $\mathbf{v}$ and the angular velocity ϕ of each particle.

(iii) Update the vertices of each particle.

(iv) Dilate the particle boundary for the inner particle stress analysis.

(v) Calculate the failure planes based on the stress state of the particle.

(vi) Calculate the shapes of the replacements for the broken particles in the current step (SSM).

(vii) Erode the new polygons based on the nonoverlapping condition.

(viii) Insert the new particles and update the contact list.

III. NUMERICAL TESTS

A simulation of the oedometric compression test is performed in this section to validate our breakage method. The performance of mass conservation and contact stability is also rigorously analyzed. The basic configuration of the particles, boundary conditions, and simulation parameters is based on the research conducted by Cantor's team [15]. They performed both experimental and numerical tests to validate the split-cell method in their paper. The bottom and side walls were rigid, and the vertical compressive load was applied at the horizontal bar located at the top of the sample. The material properties and simulation parameters—based on Cantor's tests—for the BSEM simulations in this paper are provided in Table I.

TABLE I. The material parameters and material properties for the oedometric compression test.

BSEM simulation parameters			
k_n	Normal stiffness	6.0×10^5	N/m
k_t	Tangential stiffness	2.2×10^4	N/m
μ	Friction coefficient	0.74	
Δt	Time interval	5.0×10^{-4}	s
V_d	Verlet distance	0.2	cm
Material properties			
G	Shear modulus	2.1×10^2	MPa
ν	Poisson's ratio	0.3	
ρ	Density	1.2	g/cm^2

Algorithm 1 The subset-separation method

Input:The Set has a total number of M points $\boldsymbol{p}$, $n = N$ number of fracture planes.
Output: New polygons P_i, $i = 1, \ldots, 2^N$.

for $k = 1 -> N$ **do**
  for $j = 1 -> M$ **do**
    if p_j above the kth plane **then**
      p_j assigned to subset k_α
    else if p_j below the kth plane **then**
      p_j assigned to subset k_β
    else if p_j is located on the kth plane **then**
      p_j assigned to both subset k_α and k_β
    end if
  end for
end for
for $i = 1 -> 2^N$ **do**
  S_i = intersection of subsets
  if $|S_i| < 2$ **then**
    invalid case, no polygon P_i
  else if $|S_i| > 2$ **then**
    valid case, rearrange sequences of p in S_i for P_i
  end if
end for

The particles in the original paper were made by blending plaster powder with water in the molds and drying it out in an oven; some of the material properties were not provided. The shear modulus, Poisson's ratio, and density are set according to the experiment of Jiang *et al.* [32], who used gypsumlike three-dimensional (3D) printing material for Brazilian tests. In the simulations, particles are regarded as rigid bodies. Their breakage is caused by the external compression load instead of the self-weight. Therefore, these material properties have only a minor influence on the final results. The simulations presented in this section are also performed with slightly varied parameters, and these results also support the conclusion that the material properties have only a minor influence. The critical parameters such as friction coefficient and the

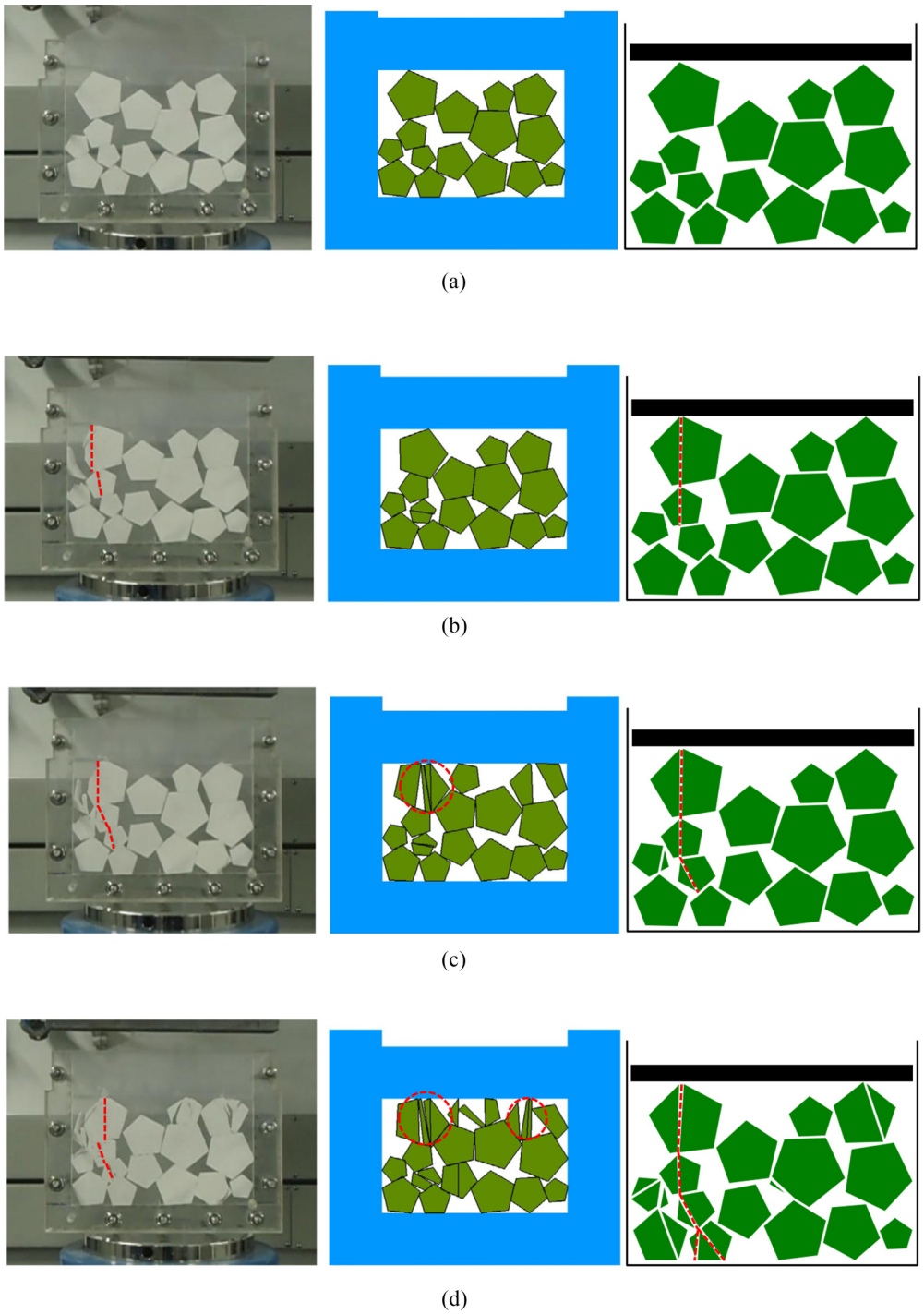

FIG. 7. The particles and fragments obtained by the DSM (right) at different times and the corresponding comparison with the experimental (left) and split-cell (middle) results obtained from Cantor *et al.* [15]. (a) $t = 0.0$ s, (b) $t = 0.9$ s, (c) $t = 1.1$ s, and (d) $t = 2.4$ s.

critical energy ϵ are set to values that are consistent with Cantor *et al.*'s research [15]. In particular, the value of $\epsilon = 2.802\,51$ MPa is numerically obtained through a Brazilian test ($r = 1.0$ cm) with the critical force ($F = 150.79$ N) that was provided in the experiment. Hence, the simulation parameters are valid and compatible with Cantor *et al.*'s experimental test. The circumdiameter of the particles ranges between 1 and 3 cm, and the rectangular container is approximately 10 cm wide and 9 cm high. The size effect on the particle strength is ignored since the difference in size between the largest and the smallest particle in the system is negligible [15].

Results of the experimental images and the split-cell method conducted by Cantor *et al.* [15] are shown at the left and middle images of Fig. 7, respectively; the corresponding simulation results of the DSM are shown in the right column. A series of characteristic fracture planes are marked out in the experimental images (left column) with dashed red lines. It can be observed from these images that the most distinctive

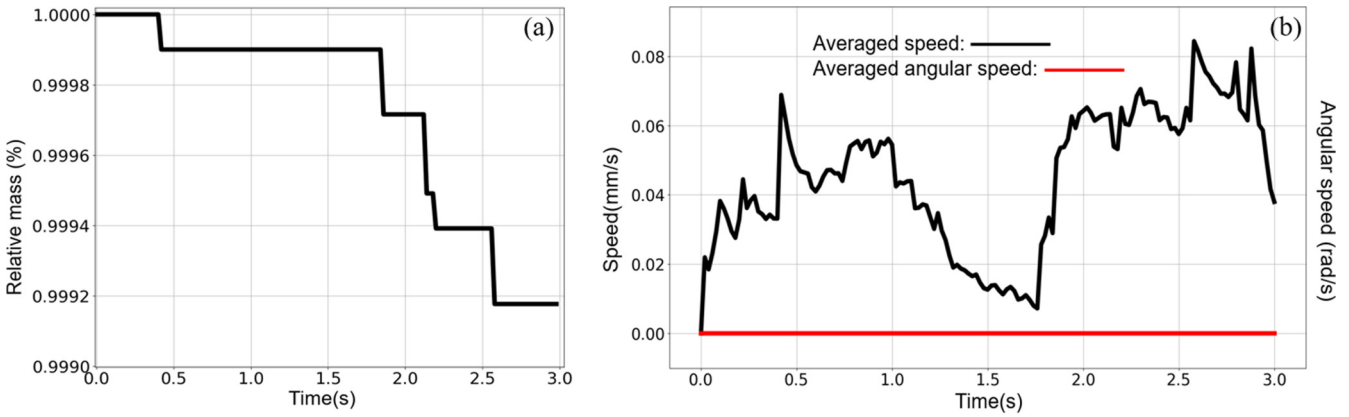

FIG. 8. (a) The variation of the total mass of the granular sample; (b) the variation of average velocity and angular velocity of the granular sample.

feature of fracture planes is that they generally form along the direction of connection lines between contact points. This relation has been observed in many laboratory studies [30]. Our previous studies [23,27] prove that contact forces govern the distribution of the inner particle strain energy field, which confines and determines the fracture planes. As the numerical implementation of this theory, the DSM properly captures this dominant feature at each measured time step. As marked out with dashed red lines in the right column of Fig. 7, the direction of fracture planes calculated by the DSM is consistent with the transmission of strain energy produced by the contact forces; both breakage locations and the geometry of new particles show a good visual match with the experiments. The split-cell method in the middle column of Fig. 7 provides less satisfactory results, which cannot properly simulate the progressive breakage along the contact pairs and force chains. Also, the split-cell method generates the so-called locking effect, as marked out in dashed red circles in Figs. 7(c) and 7(d), which repetitively breaks strip-shaped fragments from one original particle. This effect is a numerical artefact produced by the cut-in-halves strategy used in the split-cell method, and it will be further discussed in the latter part of the paper.

It needs to be noted that differences between the experiment and results of the DSM are still apparent, such as the fact that the DSM generated more fracture planes at the bottom of the container. These disagreements are mainly caused by the initial configuration in the numerical test and the plastic behavior of the experimental material, which is not perfectly elastic. Nevertheless, the simulation results show the excellent performance of the DSM, which combines the inner particle strain energy field criterion with the subset separation method as the replacement mode. Namely, the SSM enables the DSM to capture fracture planes that match well with the experimental results and avoid the locking effect. In particular, in Figs. 7(b) and 7(c) the DSM captures a series of characteristic fracture planes that occurred at the top-left area of experimental images. The split-cell method shown in the middle column of Fig. 7 does not provide an accurate result for breakage locations or fracture planes; the first breakage occurs horizontally in the middle area. Then the locking effect is generated at the top-left/right of the sample from Figs. 7(c) and 7(d), which does not occur in the results of the DSM.

It is necessary to examine the conservation of mass here since the breakage of the BSEM involves the dilation of the original particle and the erosion of the fragments. The variation of the relative mass is presented in Fig. 8(a). The number is obtained from the current total mass at a given time divided by the total mass at the beginning. Results indicate that the total mass is decreasing as the simulation progresses due to the erosion of new particles. However, our replacement method has the advantage that it conserves mass within a small variation of 0.08%, which is negligible relative to the whole granular sample. This loss of mass can also be compensated by slightly increasing the density of the particles. The small loss of mass could also be interpreted as the production of fine powder, which is often observed when breaking frictional materials.

The variation of the averaged speed and averaged angular speed is shown in Fig. 8. These values are obtained by dividing the sum of particle velocity's (or angular velocity)'s norm by the number of particles. The increase of the velocity before $t = 0.3$ s is produced by the adjustment of initial configurations to reach equilibrium on each particle and quickly dissipated by friction. The quasistatic compression begins at $t = 1.98$ s. It indicates that the fluctuations of the kinetic energy (particle velocity) are generated by the breakage events. In reality, this phenomenon is caused by the release of deformation energy and the disruption of the contact equilibrium, which is also accompanied by acoustic signals. This part of the energy distribution, as well as its dissipation, is still an open debate. In the numerical simulation, it is ideal to keep the fluctuation to a minimum for computational stability. It can be observed that the fluctuation is properly controlled and dissipated through friction. The values of average velocity are mostly below 1.0 mm/s, which is the velocity of the compression bar (loading bar at the top of the device). Numerical stability before and after the breakage is well preserved.

IV. COMPARISON WITH IRREGULAR REPLACEABLE PARTICLE METHODS

In this section, a comparison is conducted between the DSM and three other existing irregular replaceable particle methods. A two-dimensional oedometric test is adopted with

TABLE II. The breakage criteria and the corresponding cutting plane for each method. The top-left corner is the equation of averaged stress tensor $\boldsymbol{\sigma}$, where $\boldsymbol{x}^c$ is the particle centroid and $\boldsymbol{x}_n^p$ is the contact position; $\boldsymbol{F}$ is the contact force vector, $\boldsymbol{F}_{\max}$ and $\boldsymbol{F}_{\min}$ are its equivalent normal force pair; V is the particle volume, r is its circumradius, t is the unit thickness; N is the total number of contacts. σ_t and σ_s denote the tensile and shear stress; σ_1 and σ_2 are the maximum and minimum principal stress; σ_v is the von-Mises stress. σ_T and σ_C represent the uniaxial and tensile compressive strength, respectively. θ_p is the angle of the major principal plane of $\boldsymbol{\sigma}$.

$\boldsymbol{\sigma} = \frac{1}{V}\sum_{n=1}^{N}(\boldsymbol{x}^c - \boldsymbol{x}_n^p)\boldsymbol{F}_n$	Breakage criterion	Cutting planes
Split-cell method	$\sigma_t = (\lvert\boldsymbol{F}_{\max}\rvert - 3\lvert\boldsymbol{F}_{\min}\rvert)/\pi rt$ $\lvert\boldsymbol{F}_{\max}\rvert = \sigma_1\pi rt/2,\ \lvert\boldsymbol{F}_{\min}\rvert = \sigma_2\pi rt/2$ $\sigma_t > \sigma_T$	$\theta_p + \pi/2$
Cross-cut method	$\sigma_v = (\sigma_{xx}^2 + \sigma_{yy}^2 - \sigma_{xx}\sigma_{yy} + 3\sigma_{xy}^2)^{1/2}$ $\sigma_v \geqslant \sigma_c$	$\theta_p \pm \pi/4$
Mohr-Coulomb method	$(\sigma_1 < 0) \vee (\sigma_2 < 0) \vee (\sigma_2 < -\sigma_C)$ or $(\sigma_1 > 0) \vee (\sigma_2 > 0) \vee (\sigma_1 > \sigma_T)$ or $\lvert\sigma_s = (\sigma_1 - \sigma_T\sigma_2/\sigma_C)\rvert > \lvert\sigma_T\rvert$	$\theta_p + \pi/4$

a larger sample with spheropolygons generated by Voronoi tessellation. In previous papers, DEM simulations were performed using Voronoi polygons to study stress-strain response [33] and induced anisotropy [34]. This model was later extended to spheropolygons by morphological erosion of the Voronoi polygons [26]. Here we present an advanced version of these previous models that not only allows the visualization of force chains with the same resolution as in photoelastic experiments [35], but also accounts for particle fragmentation during quasistatic loading. The computational performance regarding morphological changes of individual particles and the PSD is rigorously analyzed, and the numerical effects of different particle replacement models are compared.

A. Discussion of the existing methods

The existing replaceable methods for irregular particles can be summarized into three categories based on their breakage criterion and geometrical handling mode: the split-cell method [15], the cross-cut method [14], and the Mohr-Coulomb method [16,36]. The breakage criteria and their corresponding replacement method are shown in Table II. It needs to be pointed out that the cross-cut and Mohr-Coulomb methods were originally proposed for three-dimensional cases, yet their numerical characteristics are not restricted by the number of dimensions.

An illustration of the replacement schemes is shown in Fig. 9. Notably, the averaged stress tensor $\boldsymbol{\sigma}$ is calculated based on the real contact forces $(\boldsymbol{F}_1, \boldsymbol{F}_2, \boldsymbol{F}_3)$ in Fig. 9(d), which further gives the directions of major and minor principal planes. The split-cell method first decomposes the contact forces on the particles into two pairs of opposing forces, $\boldsymbol{F}_{\max}$ and $\boldsymbol{F}_{\min}$, that are perpendicular to one another, and both cross the centroid of the particle in the direction of major ($\boldsymbol{\sigma}_{\max}$) and minor ($\boldsymbol{\sigma}_{\min}$) principal stress of $\boldsymbol{\sigma}$, respectively. The breakage is determined by the magnitudes of the equivalent forces. A broken particle will be separated along the plane of $\boldsymbol{F}_{\max}$ [Fig. 9(a)]. The cross-cut method breaks the particle based on the von-Mises stress calculated from the averaged stress tensor. A broken particle will be cut into four parts along the principal plane $\theta_p \pm \pi/4$ [Fig. 9(b)]. The Mohr-Coulomb method breaks the particle if Mohr's stress circle of the averaged stress tensor touches a predefined failure surface. The particle will be separated along the plane of $\theta_p + \pi/4$ [Fig. 9(c)]. From Figs. 9(a)–9(c), one can see that the predefined geometrical replacement mode in the split-cell method [Fig. 9(a)], the cross-cut method [Fig. 9(b)], and the Mohr-Coulomb method [Fig. 9(c)] each lead to different fracture planes (solid red lines). It is difficult to justify which approach is better since they are all solely based on the averaged stress tensor, which lacks physical meaning for the intraparticle breakage. In contrast, our DSM method

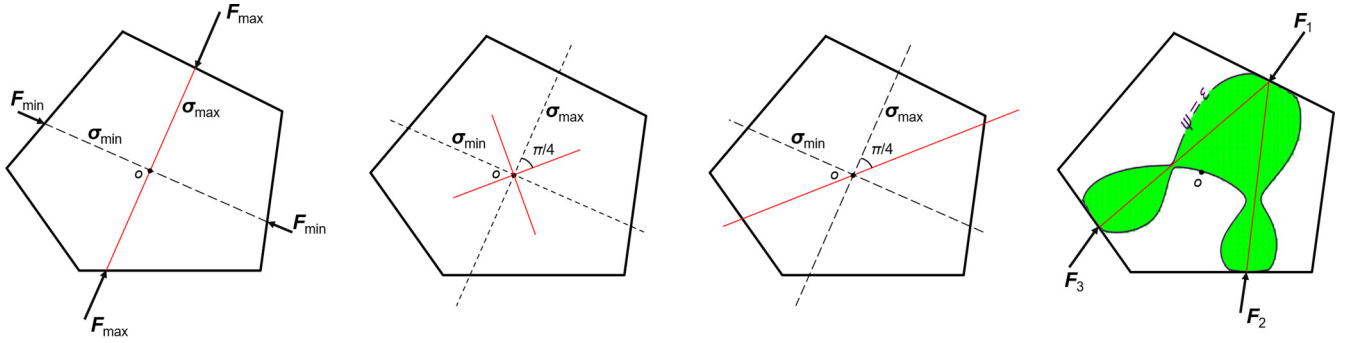

FIG. 9. The replacement method used for each replaceable particle method. The actual contact forces are shown in (d) along with the results of DSM. (a) The split-cell method, (b) the cross-cut method, (c) the Mohr-Coulomb method, and (d) the damaged-separation method.

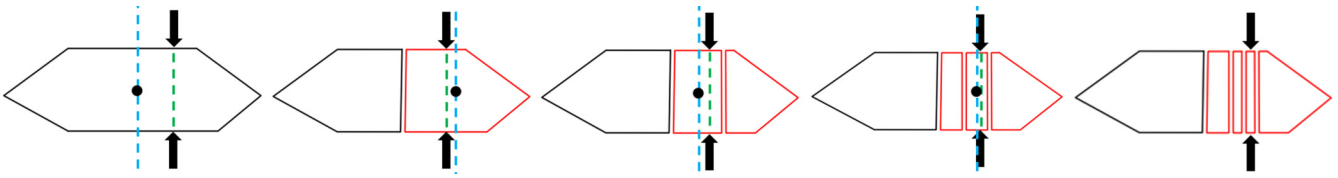

FIG. 10. The scheme of the "locking effect" generated by the replacement mode in the split-cell method. Black arrows are loading forces; black dots denote the centroid of the polygon; blue lines and green lines are the fracture planes and connection lines between contact points, respectively.

calculates the inner particle stress field of the particle and uses this to predict the fracture planes [Fig. 9(d)]. Hence, our method is based on more realistic physics because it requires none of the nonunique assumptions of the other three methods to obtain the fracture planes. The only simplification of our method is that the fracture plane is straight, whereas, in reality, the geometry of the fracture may be more complicated.

It can be seen that existing methods rely solely on the averaged stress tensor for determining the breakage and shape of the replacements. These criteria, whether the maximum tensile stress, Mohr-Coulomb failure surface, or von-Mises stress, often fail to properly represent the breakage process as the averaged stress tensor oversimplifies the stress state of the particle [23,27]. Meanwhile, the replacement modes of the existing methods are also problematic since the fracture planes are restricted to pass through the centroid of the original particle.

For the split-cell method, this restriction commonly causes one of the postbreakage particles to bear the same load as the original particle. As shown in Fig. 10, the contact forces are preserved after the replacement, and the force equilibrium is maintained since the fracture plane always crosses the centroid. Breakage is locked by this numerical effect. In reality, a breakage event alters the force equilibrium and causes a decrease or disappearance of the original contact forces through the rearrangement of the fragments. The cut-into-halves strategy used by the split-cell method cannot properly capture this process and suffers from this numerical error. This "locking effect," as mentioned earlier in this paper, was addressed by Eliáš [14] when he formulated the cross-cut method to avoid this issue. As an improvement, the shearinglike separation strategy used by the cross-cut and Mohr-Coulomb methods attenuates this issue by allowing new particles to rearrange through sliding after the replacement. The original contact forces can be slowly dissipated with the rearrangement of new particles. However, the effectiveness of this approach is sensitive to an increase in the frictional coefficient. The DSM separates the particles along the line determined by the strain energy field governed by the contact forces. The centroid is no longer a restriction on the fracture planes. As illustrated in Fig. 6, the original contact forces, as well as the force equilibrium, are canceled out through the erosion after the replacement. The fragments are allowed to rearrange to a new static state.

Geometrical patterns generated by the replacement modes also need to properly simulate the morphological changes of broken particles, which would strongly affect the accuracy of the PSD. A representative laboratory study was conducted by Karatza *et al.* [28] using x-ray tomography to reveal the breakage progress of spherical particles in the oedometric test. They identified three breakage types that are commonly observed in their experiment: chipping, splitting, and fragmentation. The types are further illustrated in Fig. 11.

Existing replacement modes can only simulate one of the breakage types. The split-cell method and the Mohr-Coulomb method can only produce splitting since the cut-into-halves strategy is used for the replacements. The cross-cut method can only produce fragmentation type of fragmentation because a broken particle is always cut along the planes crossing at the centroid. The DSM can produce all three breakage types since it has no restriction on the number or the location of the cutting planes.

Breakage types calculated based on each method are presented in Fig. 12. The results further demonstrate that the DSM correctly produces the corresponding breakage type based on the loading conditions for $N = 2, 3, 4$. For a coordination number $N = 2$, the split-cell method and the Mohr-method provide the split type of breakage, both the number and the shape of the fragments are properly approximated. The DSM also produces the split type of breakage, but the mass ratio between two fragments is more realistic. The cross-cut method fails to provide a good result due to the nature of its replacement method. For coordination number $N = 3, 4$, the cross-cut method has better performance than the other two methods since the fragmentation breakage type, as observed in the x-ray experiment [28], is far more common than the split type of breakage. However, the cross-cut method still cannot produce the chipping type of breakage that ranked as the second most frequent breakage type [28]. The DSM can produce the chipping type of breakage if the concentration of contact forces is located near the boundary of the particle. This phenomenon is further illustrated in Fig. 12 for $N = 4$.

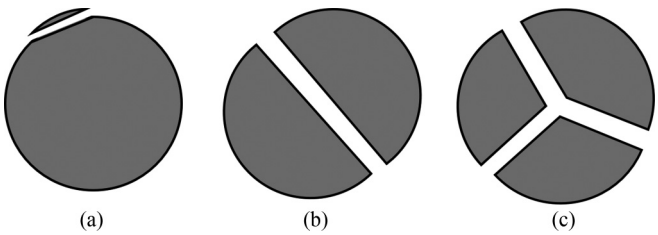

FIG. 11. The three breakage types: chipping, splitting, and fragmentation. (a) chipping, two fragments have extremely different sizes generated from the concentration of the contact forces near the boundary. (b) splitting, the particle is separated into two roughly equal parts. (c) fragmentation, the particle is separated into three or more roughly equal parts.

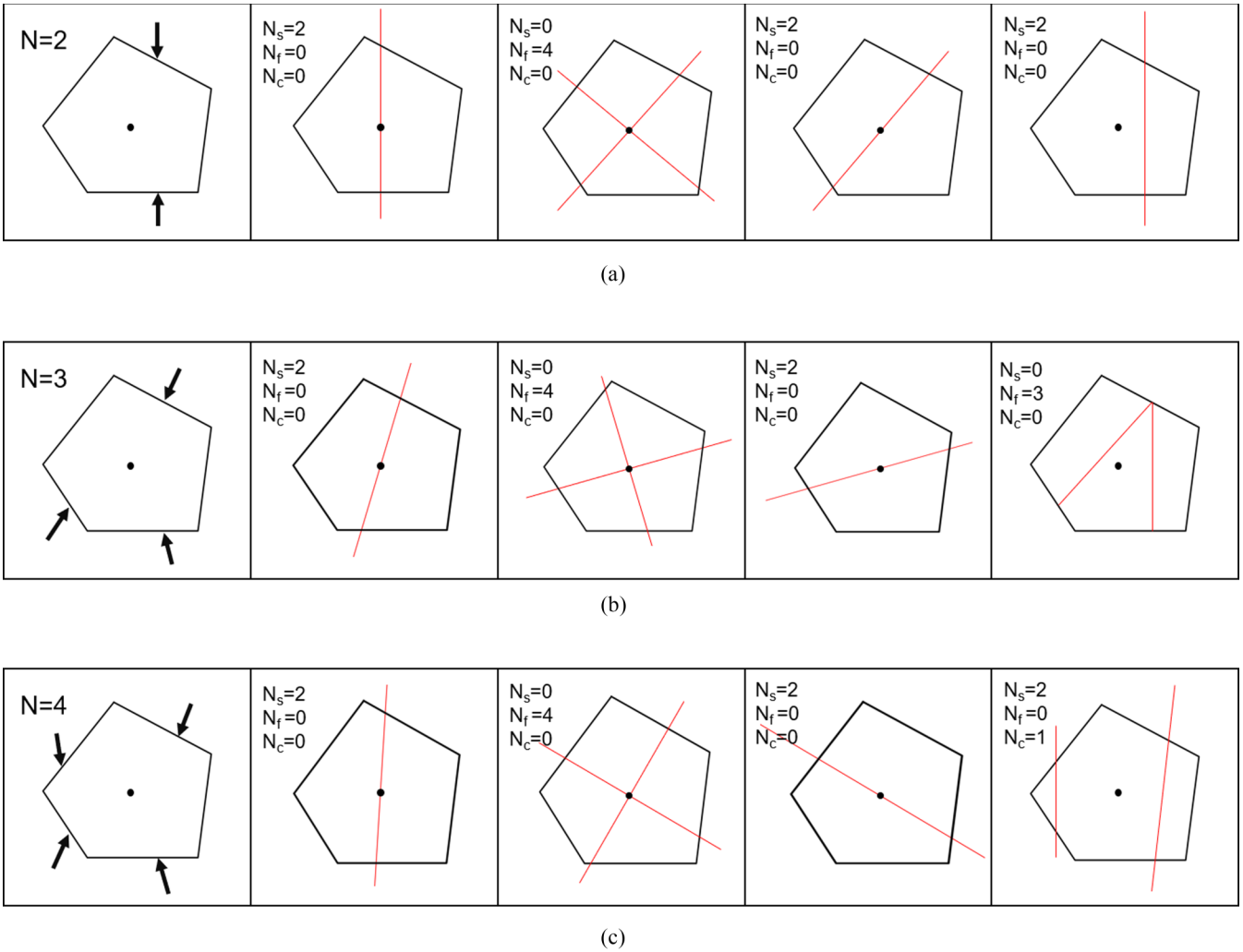

FIG. 12. The breakage types generated with different replacement methods under various loading conditions and coordination numbers. The first column is the loading configuration with black arrows. The second column shows the results of the split-cell method. The third column is the results of the cross-cut method. The fourth column is the Mohr-Coulomb method. Results in the last column are produced by the DSM. The subscripts s, f, and c denote the breakage types of splitting, fragmentation, and chipping. (a) $N = 2$, (b) $N = 3$, and (c) $N = 4$.

B. Oedometric test with Voronoi spheropolygons

Oedometric tests are performed with the four methods specified above (split-cell method, cross-cut method, Mohr-Coulomb method, and our damaged-separation method) to further validate their differences and advantages. The sample is generated with a Voronoi tessellation and is packed with gravity before the loading test. The packing sample is 137 cm wide and roughly 110 cm high. Simulation parameters are the same as in Table I, except for the frictional coefficient $\mu = 0.4$. The compressive bar is assigned with a constant velocity $v_y = -1.0$ mm/s for 10.0 s.

The final breakage for each method is presented in Figures 13(a)–13(d), which contain zoomed figures of the broken particles. As discussed earlier, the split-cell suffers from the locking effect in Fig. 13(a). The strip-shaped fragments are repetitively produced in a local region. This unrealistic pattern severely compromises the accuracy of the split-cell method for calculating the breakage effect on both the micro- and macroscale. It can be observed from Figs. 13(b) and 13(c) that the cross-cut and Mohr-Coulomb methods both mitigated this problem by allowing the particle to slide along the cutting plane. The DMS does not have the issue of the locking effect since the forces are canceled by the new replacements [Fig. 13(d)], which allows the local particles to be rearranged to a new force equilibrium.

The final spatial distributions of fragments for each test are shown in Figs. 14(a)–14(d) based on their centroids. It can be observed in Figs. 14(a) and 14(b) that the split-cell method and the cross-cut method both have the problem of localization of the breakage events. Most of the breakage events occur within a vertical or horizontal narrow band. Particle breakage should be progressively spread with the contact force transmission, which is induced by the compressive pressure, inside the granular packing. This strong directional localization of breakage events does not represent a realistic mechanical behavior, but a numerical artefact created by the geometrical replacement modes. As we can see, the results provided by the Mohr-Coulomb method and the DSM in Figs. 14(c) and 14(d) are quite similar. Distributions of fragments are not localized in a particular region or direction.

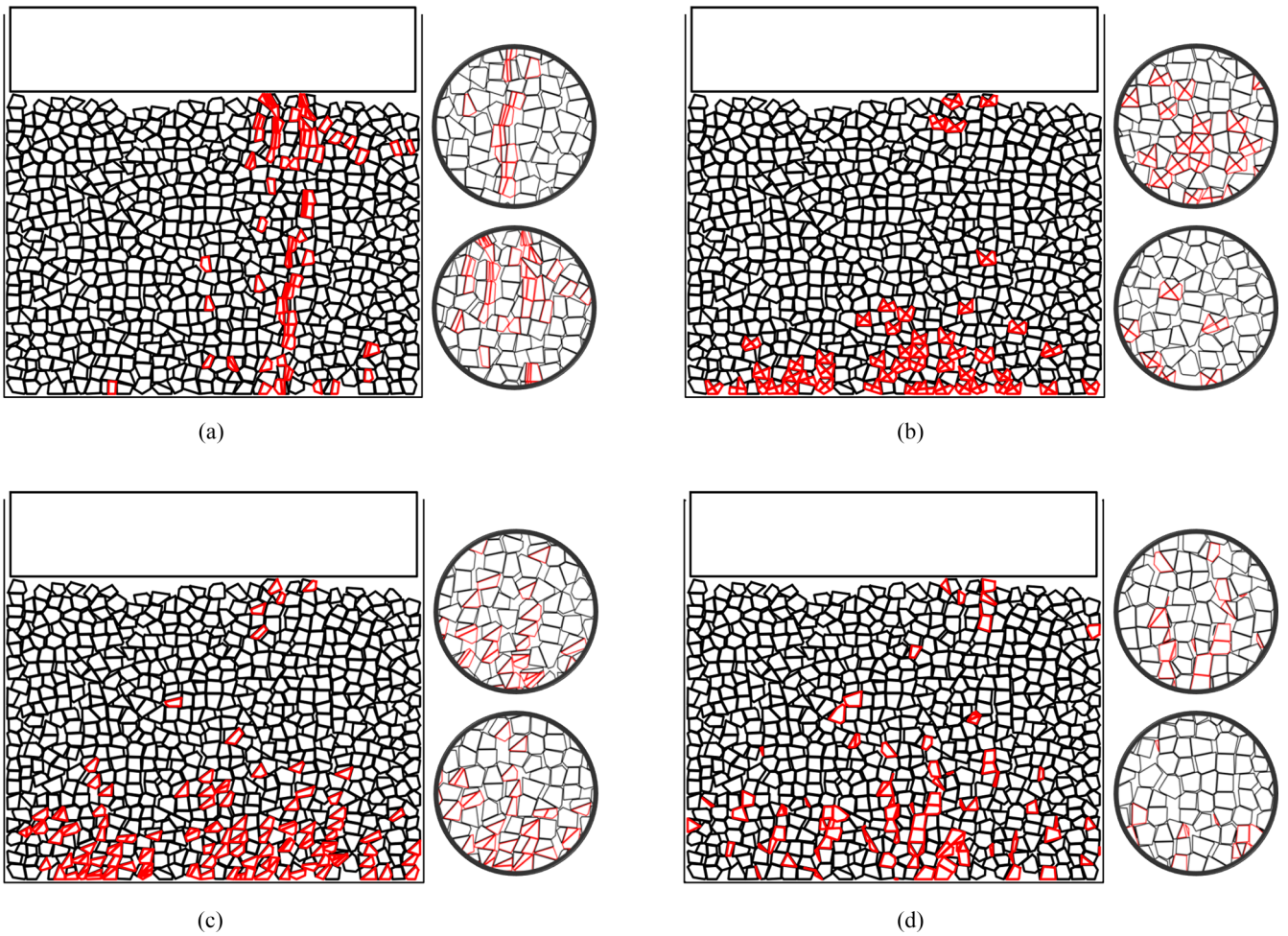

FIG. 13. Final breakage patterns of particles simulated with each replaceable particle method. The black color represents the intact and original particles; the red color represents the new replacements. (a) The split-cell method, (b) the cross-cut method, (c) the Mohr-Coulomb method, and (d) the DSM method.

The orientation of fracture planes (which ranged from 0° to 360°) is another indicator of whether the morphological changes caused by particle breakage are correctly simulated. Fracture planes determine the shape and mass of the new fragments, which would further affect the PSD and the evolution of the force chain network. The directional frequency of fracture planes in each test is shown using polar histograms in Figs. 15(a)–15(d). The results indicate that all the methods, which adopted the centroid as the constraint in the geometrical replacement mode, have a strong polarizing pattern. The orientation of fracture planes has one or two dominating angles. For the split-cell method, the angle is nearly 90°/270° with the highest frequency of 10. For the cross-cut and Mohr-Coulomb methods, the fracture orientations concentrate along two angles (15.2°/195°, 105.2°/275.2°) and (45.6°/225.6°, 157.3°/337.3°) with the highest frequency

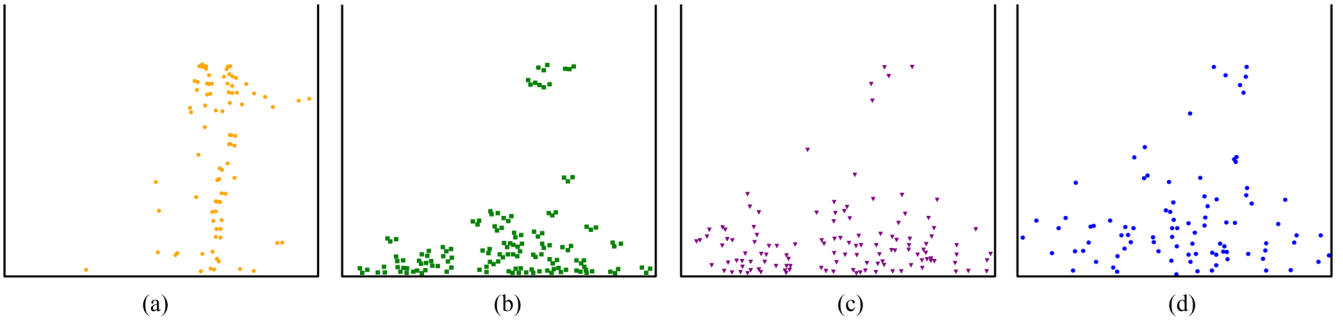

FIG. 14. Spatial distribution of the fragments generated by each method: (a) the split-cell method, (b) the cross-cut method, (c) the Mohr-Coulomb method, and (d) the DSM method.

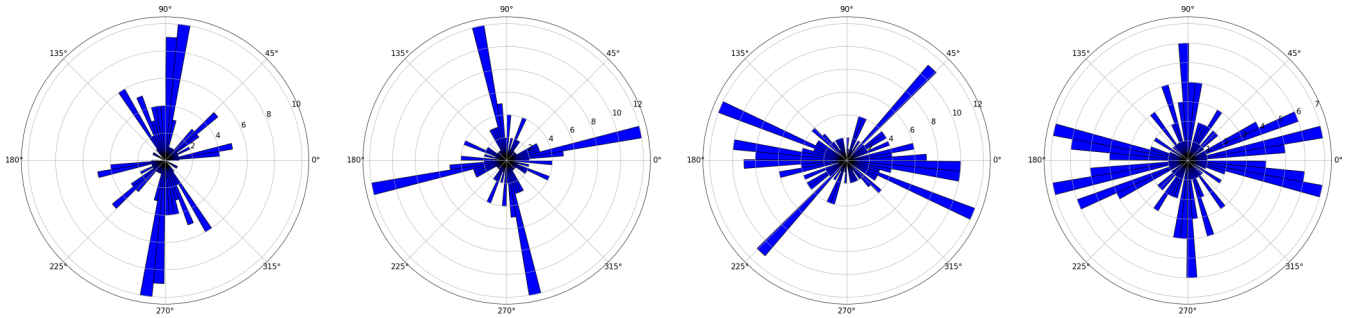

FIG. 15. The directional frequency of fracture planes in each replaceable particle method: (a) the split-cell method, (b) the cross-cut method, (c) the Mohr-Coulomb method, and (d) the DSM method.

of 12°. The inadequacy of the centroid constraint is the main reason for the numerical polarization of fracture planes. Meanwhile, the averaged stress tensor used by these methods oversimplifies the actual stress field that governs the fracture planes. Hence, the orientation of fracture planes at the particle scale tends to be consistent with the fracture angle calculated as if the granular packing is one whole continuum. For the DSM, this polarization is much weaker than the other three methods with the highest frequency of 7°. This is because its geometrical replacement mode does not have a predefined limitation, and the fracture planes are determined based on the inner particle strain energy field.

The results of the PSD generated by each method are shown in Fig. 16. In particular, the PSD of the cross-cut method has a clear "lump" at the encircled part. It is caused by the fact that the particles are always separated into four particles of similar size and produce a concentration in the particle sizes [14]. This problem makes the cross-cut method less appropriate to reproduce the breakage effect at the macroscale. The other three methods produced a relatively similar result. The main difference is the tail of the PSD, where the DSM generated more particles that are smaller than 1.5 cm and thus has a longer tail. It indicates that the DSM has a better ability to capture the generation of small particles and produce a more realistic PSD.

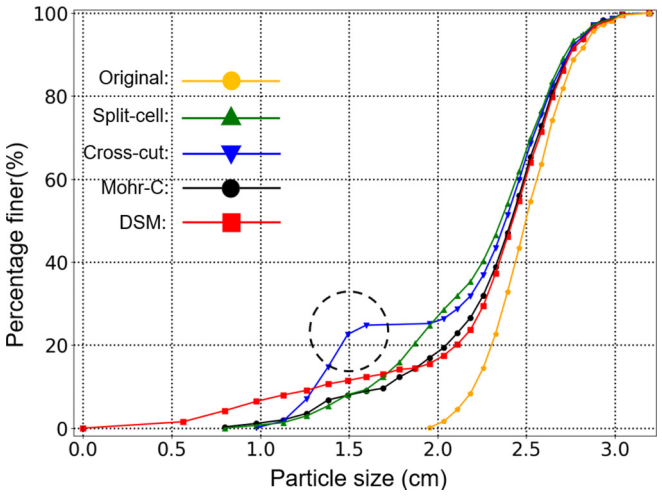

FIG. 16. The particle size distribution provided by the replacement methods. The black dashed circle marks out the lump that is numerically caused by the cross-cut method.

To further examine this feature of the DSM, the percentage of the different breakage types generated by the DMS is shown in Table III. The definition of each type is identified through the mass ratio m_r of fragments. The value of m_r is calculated as $m_r = m_{\text{fra}}/m_{\text{aver}}$, where m_{fra} and m_{aver} represent the minimum mass of the fragment and the averaged mass of particles at the initial time. It can be seen that fragmentation and chipping are the dominant breakage types, which occupy 45.6% and 50.06% of the total breakage events, and splitting occupies only 4.34% of the total breakage events. This result is consistent with the experimental data of Karatza *et al.* [28]. Therefore, the long tail of PSD mainly consists of the chipping and fragmentation types of breakage, which can be regarded as a more realistic result of oedometric compression.

By removing the limitation of using the particle centroid in the breakage, the DMS provides all three breakage types: chipping, splitting, and fragmentation. In particular, the percentage of the fragmentation and the chipping can be simulated since the cutting line is determined based on the strain energy field. These attributes allow the DSM to be used to study the morphological changes due to fragmentation, while the other methods can only produce a single type of breakage and do not fully recognize the important link between the cutting plane and the contact position.

As a final validation of our simulation results, we numerically plotted the force chain network inside the granular material [23,24]. Figures 17(a) and 17(b) show the overall, as well as the zoomed, visualization of the standard photoelastic quantity $I = (\sigma_1 - \sigma_2)$, where σ_1 and σ_2 denote the maximum and minimum principal stress on each particle. The calculation is conducted at $t = 7.0$ s in the DSM simulation to have fully transmitted force chains. The contact between the compression bar and the granular packing first occurs at the right side due to the initial configurations, where the root of

TABLE III. The percentage of each breakage type in the DSM simulation as a function of the mass ratio of the fragments.

Breakage types	Splitting	Fragmentation	Chipping
Mass ratio m_r	$m_r > 0.4$	$0.4 \geqslant m_r \geqslant 0.1$	$0.1 > m_r$
Percentage	45.6%	50.06%	4.34%

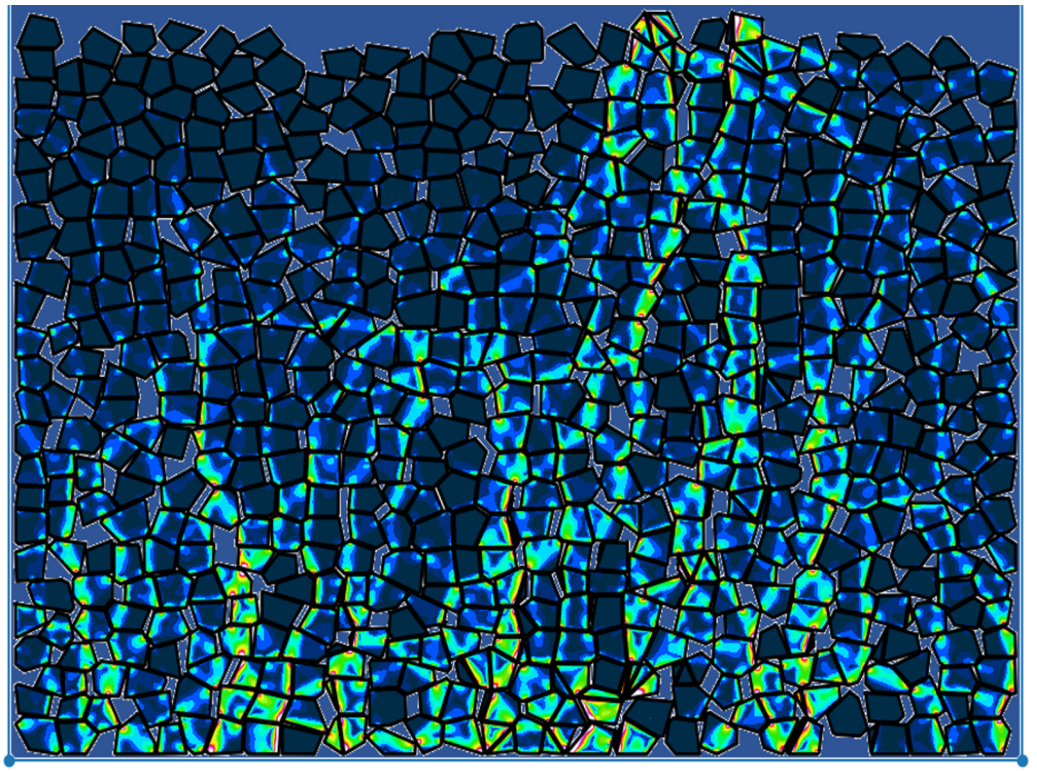

(a)

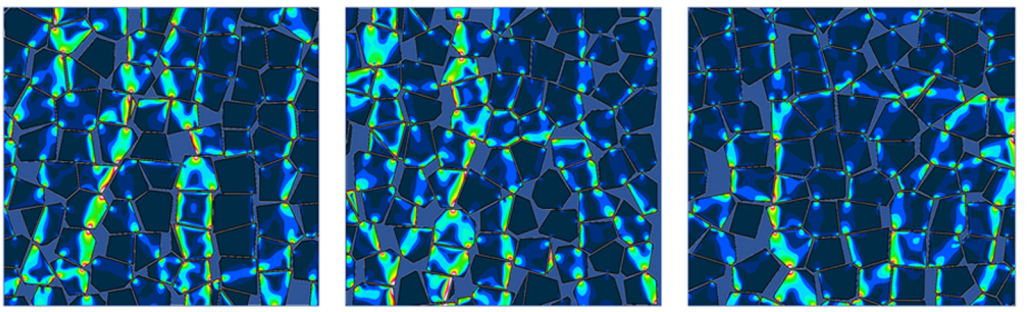

(b)

FIG. 17. (a) The force chain network $I = (\sigma_1 - \sigma_2)$ of the granular sample and (b) zoomed areas. The calculation is conducted at $t = 7.00$ s in the test of the DSM.

the force chain network is located. Figure 17 indicates that the spatial distributions of fragments, fracture planes, and broken particles in the DSM method are perfectly consistent with the force chain network.

V. CONCLUSIONS

In this paper, we implemented a replaceable particle method, namely the damage-separation model (DSM), to the boundary-spheropolygon element method (BSEM) for simulating particle breakage. This is a highly efficient and high-resolution DEM model that allows fragmentation based on the internal stress field of the particles. More precisely, the breakage criterion is governed by the inner particle strain energy field. The replacement scheme of the new particles is then determined by the connection points—calculated from the strain energy—and the position of the contact points. This method has unique advantages for simulating the fundamental mechanism of particle breakage at both the individual particle and granular level.

A geometrical algorithm, namely the subset separation method (SSM), is developed and incorporated into the DSM to handle the recognition and replacement of fragments. This algorithm allows a convex polygon to be cut based on a set of arbitrary cutting lines. The algorithm removes previous artificial restrictions on the number of fragments and the orientation of fracture planes that is used in current approaches based on the averaged stress tensor. The SSM enables the DSM to better simulate the morphological changes of new particles.

Oedometric compression tests based on the existing literature and Voronoi diagrams are performed as validation and

demonstration of the breakage method at the granular level. The conservation of mass is well preserved, and the numerical stability of the breakage is properly maintained. A comparative study using different replaceable particle methods is further conducted and indicates that the DSM shows the best performance for simulating the breakage process. The DSM avoids the numerical errors of the locking effect, the polarization of fracture planes, and the lump in the PSD that occur in average-stress-tensor-based approaches. All three breakage types observed from the experimental data can be simulated using the DSM, and morphological changes are correctly captured using the SSM.

In conclusion, the advantage of the DSM is the preservation of the physical information during particle breakage and reduction of the interference of artificial effects in the numerical simulation. It gains its superior accuracy by using the inner particle stress field to determine breakage, largely removing the use of empirical parameters and the limitations of the geometry of the replacements. The authors expect the DSM to make a lasting contribution to the study of the mechanism of particle breakage.

ACKNOWLEDGMENTS

This research is financially supported by the Australian Research Council (ARC) linkage project "Performance of granular matrix under heavy haul cyclic loading" (LP160100280). The authors also thank Buddhima Indraratna from the University of Technology Sydney for the critical discussion. We also thank the anonymous reviewers for their critical comments. F. Alonso-Marroquín expresses his gratitude to Professor Ioannis Vardoulakis, who inspired this work.

[1] M. Koohmishi and M. Palassi, Rock Mech. Rock Eng. **49**, 2655 (2016).
[2] G. Miao and D. Airey, Géotechnique **63**, 1221 (2013).
[3] B. O. Hardin, J. Geotech. Eng. **111**, 1177 (1985).
[4] F. Altuhafi and M. R. Coop, Géotechnique **61**, 459 (2011).
[5] F. Altuhafi, B. A. Baudet, and P. Sammonds, Soils Found. **51**, 113 (2011).
[6] G. McDowell, M. Bolton, and D. Robertson, J. Mech. Phys. Solids **44**, 2079 (1996).
[7] K. L. Lee and I. Farhoomand, Can. Geotech. J. **4**, 68 (1967).
[8] A. B. Kh, A. Mirghasemi, and S. Mohammadi, Powder Technol. **205**, 15 (2011).
[9] D. André, I. Iordanoff, J.-l. Charles, and J. Néauport, Comput. Methods Appl. Mech. Eng. **213-216**, 113 (2012).
[10] J. de Bono and G. McDowell, Géotechnique **66**, 1014 (2016).
[11] B. Wang, U. Martin, and S. Rapp, Comput. Geotech. **88**, 61 (2017).
[12] J. A. Åström and H. J. Herrmann, Eur. Phys. J. B **5**, 551 (1998).
[13] O. Tsoungui, D. Vallet, and J.-C. Charmet, Powder Technol. **105**, 190 (1999).
[14] J. Eliáš, Powder Technol. **264**, 458 (2014).
[15] D. Cantor, N. Estrada, and E. Azéma, Comput. Geotech. **67**, 150 (2015).
[16] A. Gladkyy and M. Kuna, Gran. Matter **19**, 41 (2017).
[17] G. McDowell and O. Harireche, Géotechnique **52**, 299 (2002).
[18] G. Ma, W. Zhou, and X.-L. Chang, Comput. Geotech. **61**, 132 (2014).
[19] G. Ma, W. Zhou, R. A. Regueiro, Q. Wang, and X. Chang, Powder Technol. **308**, 388 (2017).
[20] F. Zhu and J. Zhao, Géotechnique **69**, 526 (2019).
[21] L. F. Orozco, J.-Y. Delenne, P. Sornay, and F. Radjai, Int. J. Solids Struct. **166**, 47 (2019).
[22] J. P. de Bono and G. R. McDowell, Int. J. Solids Struct. **187**, 133 (2020).
[23] Y. Jiang, H. J. Herrmann, and F. Alonso-Marroquin, Comput. Geotech. **113**, 103087 (2019).
[24] Y. Jiang and F. Alonso-Marroquin (unpublished).
[25] F. Alonso-Marroquín and Y. Wang, Gran. Matter **11**, 317 (2009).
[26] S. A. Galindo-Torres, J. D. Muñoz, and F. Alonso-Marroquin, Phys. Rev. E **82**, 056713 (2010).
[27] Y. Jiang, F. Alonso-Marroquín, H. J. Herrmann, and P. Mora, Gran. Matter **22**, 69 (2020).
[28] Z. Karatza, E. Andò, S.-A. Papanicolopulos, G. Viggiani, and J. Y. Ooi, Gran. Matter **21**, 44 (2019).
[29] P. V. Lade and H. Karimpour, Int. J. Solids Struct. **87**, 167 (2016).
[30] R. Artoni, A. Neveu, Y. Descantes, and P. Richard, J. Mech. Phys. Solids **122**, 406 (2019).
[31] B. Chazelle and D. P. Dobkin, in *Machine Intelligence and Pattern Recognition* (Elsevier, Amsterdam, 1985) Vol. 2, pp. 63–133.
[32] C. Jiang, G.-F. Zhao, J. Zhu, Y.-X. Zhao, and L. Shen, Rock Mech. Rock Eng. **49**, 3983 (2016).
[33] F. Alonso-Marroquin and H. J. Herrmann, Phys. Rev. E **66**, 021301 (2002).
[34] F. Alonso-Marroquin, S. Luding, H. J. Herrmann, and I. Vardoulakis, Phys. Rev. E **71**, 051304 (2005).
[35] L. Vanel, D. Howell, D. Clark, R. P. Behringer, and E. Clément, Phys. Rev. E **60**, R5040(R) (1999).
[36] P. S. Iliev, F. K. Wittel, and H. J. Herrmann, Phys. Rev. E **99**, 012904 (2019).